Journal of Materials Chemistry A

ROYAL SOCIETY OF CHEMISTRY

PAPER

Cite this: *J. Mater. Chem. A*, 2025, **13**, 38252

Revealing the role of grain boundaries in magnesium-based hydrogen storage: insights into adsorption and dissociation

Xiaotian Tang,[ab] Jianghao Cai,[ab] Tongao Yao,[ab] Zhuoran Xu,[ab] Yuxuan Liu,[ab] Ziwei Miao,[ab] Chu Wang,[ab] Man Shu,[ab] Kewen Guo,[ab] Zhengyang Gao,[ab] Xuqiang Shao[c] and Weijie Yang *[ab]

Mg is an attractive hydrogen storage material, yet its practical application is hindered by sluggish hydrogen uptake due to high H_2 dissociation barriers. Although experiments suggest that grain boundaries (GBs) serve as preferential sites for hydride nucleation, the atomic-scale mechanisms remain unclear. In this paper, we employed density functional theory (DFT) calculations to elucidate hydrogen adsorption and dissociation at representative Mg twin boundaries with different misorientation angles. We found that hydrogen adsorption consistently favors Hollow sites at GBs owing to strong Mg–H orbital hybridization. Among the studied configurations, the $\{10\bar{1}1\}$ twin boundary exhibits the lowest dissociation barrier (0.74 eV), reduced by 34.5% compared with Mg (0001). Strikingly, the dissociation barriers follow a non-monotonic "reversed volcano" trend with GB rotation angle, where intermediate-angle GBs maximize charge transfer into the H_2 σ^* orbital and thereby facilitate bond cleavage. This synergy between local free volume, coordination number, and electronic redistribution provides a unified descriptor (χ_{gem}) that rationalizes the angular dependence of reactivity. Our findings establish a clear mechanistic link between GB geometry and hydrogen activation, offering design principles for tailoring microstructures to accelerate hydrogen storage kinetics in Mg-based materials.

Received 16th June 2025
Accepted 30th September 2025

DOI: 10.1039/d5ta04858c

rsc.li/materials-a

1 Introduction

Magnesium-based hydrogen storage materials are regarded as some of the most promising candidates due to their non-toxicity, low cost, and high hydrogen storage capacity (up to 7.6 wt%).[1–4] However, the slow rate of hydrogen absorption and release, the easy formation of a dense passivation layer on the surface, and the high temperature of hydrogen release due to the stability of hydrides have limited their application in practice.[2,5,6] Recent advances in magnesium-based hydrogen storage materials have focused on optimizing absorption/desorption kinetics through three principal approaches: catalytic doping, structural nanocrystallization, and alloy engineering. For example, recent studies have shown that an *in situ* reaction between MgH_2 and a CuNi alloy during dehydrogenation can generate a Mg_2Ni(Cu) ternary alloy, thereby enabling the synergistic integration of photothermal and catalytic effects within a single phase.[4,7–9] This atomic reconstruction strategy not only significantly enhances broadband light absorption and local heating efficiency, but also weakens the Mg–H bonds and lowers the hydrogen diffusion barriers, thus markedly improving the kinetic performance of MgH_2. In addition to alloy design, the most successful strategies also include mechanical processing of powders *via* high-energy ball milling (HEBM) and defect engineering through severe plastic deformation (SPD). On the one hand, nanostructured materials produced by HEBM have exhibited significantly enhanced hydrogen absorption/desorption kinetics, although they are often susceptible to surface contamination. On the other hand, SPD techniques offer the unique advantage of tailoring GBs while minimizing surface contamination, and several SPD methods have indeed demonstrated effectiveness in producing materials with accelerated hydrogen absorption/desorption kinetics.[10]

GBs are widely recognized as accelerated "diffusion highways" in various materials, and they play a similar role in hydrogen diffusion by promoting hydrogen trapping at defect sites.[11,12] Karst *et al.*[13] pioneered real-time nanoscale visualization of hydrogen diffusion kinetics in magnesium thin films using scattering scanning near-field optical microscopy (s-SNOM), specifically tracking the Mg → MgH_2 phase transition dynamics at GBs. Their breakthrough observations revealed preferential hydride nucleation at GB interfaces, thereby validating the hypothesized role of GBs as rapid hydrogen transport

[a]*Department of Power Engineering, North China Electric Power University, Baoding 071003, Hebei, China. E-mail: yangwj@ncepu.edu.cn*

[b]*Hebei Key Laboratory of Energy Storage and Integrated Energy Systems, North China Electric Power University, Baoding 071003, Hebei, China*

[c]*Department of Computer, School of Control and Computer Engineering, North China Electric Power University, Baoding 071003, China*

channels. However, while dynamically demonstrating GBs as hydrogenation initiation sites, the study did not establish systematic correlations between GB atomic configurations (*e.g.*, misorientation angles/dislocation densities) and corresponding hydrogen interaction mechanisms.

Hydrogen embrittlement of Mg has been experimentally and theoretically linked to its grain boundaries. Chino *et al.*[14] showed that even ppm-level hydrogen segregates preferentially at triple junctions, raising the ductile-to-brittle transition temperature and promoting intergranular fracture. Complementarily, Yuasa *et al.*[15] demonstrated through first-principles simulations that hydrogen segregation at a $\{11\bar{2}4\}$ TB strengthens local Mg–H bonds but simultaneously suppresses dislocation emission, thereby enhancing crack propagation. These findings confirm the critical role of GBs in hydrogen behavior, but remain limited to specific GB types. The broader question of how distinct GB configurations and misorientation angles regulate hydrogen adsorption and dissociation remains open, motivating the present systematic investigation.

The profound influence of GBs in magnesium hydride nucleation prompts a fundamental materials science inquiry: which GB configurations preferentially mediate hydride formation? To address this issue, we employed first-principles DFT calculations to unravel the dissociation pathways of H_2 on representative Mg GB surfaces. This investigation focused on magnesium's symmetric tilted grain boundaries (STGBs). In constructing the GB structures, we adopted a methodology[15,16] to systematically model TBs for several common rotation angles. Building upon these models, we conducted comprehensive analyses of hydrogen adsorption and H_2 dissociation processes at distinct surface sites, thereby elucidating the dissociation and adsorption characteristics of H_2 on each GB surface. To unravel the underlying mechanisms, we quantified the Bader charge transfer between hydrogen and the GB surfaces during adsorption and systematically investigated how the unique structural features of GBs influence hydrogen dissociation dynamics.

2 Computation methods

All DFT calculations were performed using the Vienna *Ab Initio* Simulation Package (VASP). The relevant interactions were calculated using the generalized gradient approximation (GGA) with the Perdew–Burke–Ernzerhof (PBE) functional.[17] The adjustments of van der Waals interaction were taken into account by using the DFT-D3 framework.[18] After testing various cutoff energies and *k*-point meshes by comparing CPU times and free energy differences, we finally adopted a plane-wave basis set with an energy cutoff of 500 eV to describe the valence electrons, together with a Γ-centered $3 \times 3 \times 1$ *k*-point mesh for structural relaxations. The convergence criterion of the interatomic force was 0.02 eV Å^{-1} when optimizing the structure. In the self-consistent calculation, the energy difference between each electronic step was considered to have reached the convergence criterion when it was 10^{-5} eV.

The adsorption energy of a H atom on the surface was calculated according to the following equation:

$$E_{\text{ads-H/Mg}} = E_{\text{H/Mg}} - (E_{\text{Mg}} + E_{\text{H}}) \quad (1)$$

where $E_{\text{H/Mg}}$ is the total energy of a single hydrogen atom adsorbed on the surface of magnesium, E_{Mg} is the total energy of magnesium, and E_{H} is the total energy of a free hydrogen atom. The negative adsorption energy indicates that the adsorption system is more stable than the single-component system, and the smaller the negative value, the more stable the configuration of the adsorbed H atom.

To determine the transition state (TS) structure during the simulation process, the climbing image nudged elastic band (CI-NEB) method[19,20] was initially employed to estimate the TS. This was followed by precise optimization of the obtained TS using the improved dimer method (IDM).[21] The force convergence criterion for the IDM method was set to 0.02 eV Å^{-1}. To validate the accuracy of the TS, vibrational frequency analysis was conducted with a displacement constraint of $\pm$0.02 Å.[22] We used the relevant functions of OVITO[23] to calculate the coordination number (CN) and Voronoi volume of Mg atoms at each GB. We performed ELF analysis using the VESTA visualization system to characterize the chemical bonding topology;[24] carried out DOS calculations with the VASPKIT package for electronic structure interpretation,[25] and conducted Bader charge analysis to evaluate the charge transfer during H adsorption and the charge distribution on the GB surfaces.

3 Results and discussion

3.1 Computational models

Although the hexagonal close-packed (HCP) structure is one of the most common crystal structures in structural materials, its deformation modes are much more complex compared with those of body-centered cubic (BCC) and face-centered cubic (FCC) crystals. For crystalline materials, the parent lattice must provide at least five independent deformation modes to accommodate arbitrary plastic strains, according to the Taylor–von Mises criterion. While FCC and BCC systems readily satisfy this requirement through a sufficient number of slip systems, HCP crystals can activate fewer than five independent slip modes at room temperature. Consequently, deformation in HCP materials is governed primarily by a combination of slip and twinning, which explains the frequent occurrence of deformation twins in such systems.[26,27] In constructing the GB models, we focused on symmetric tilt boundaries with relatively low formation energies, as such boundaries are thermodynamically more stable and more likely to be observed experimentally. Therefore, several GBs with misorientation angles in the range of 0–90° were selected.[28–32] It should be noted that, unlike FCC or BCC systems, where common planes can be straightforwardly constructed, Mg GBs are more complex. For example, as shown in Fig. 1a, the $\{10\bar{1}2\}$ twin boundary plane exhibits a "corrugated" configuration.[16] The construction of such twins requires additional lattice shifts to avoid excessively short interatomic distances at the interface. In practice, this represents an approximate approach to GB construction, and as a result, the optimized structures may exhibit a slight deviation in the rotation angle compared with the actual GBs. To mitigate

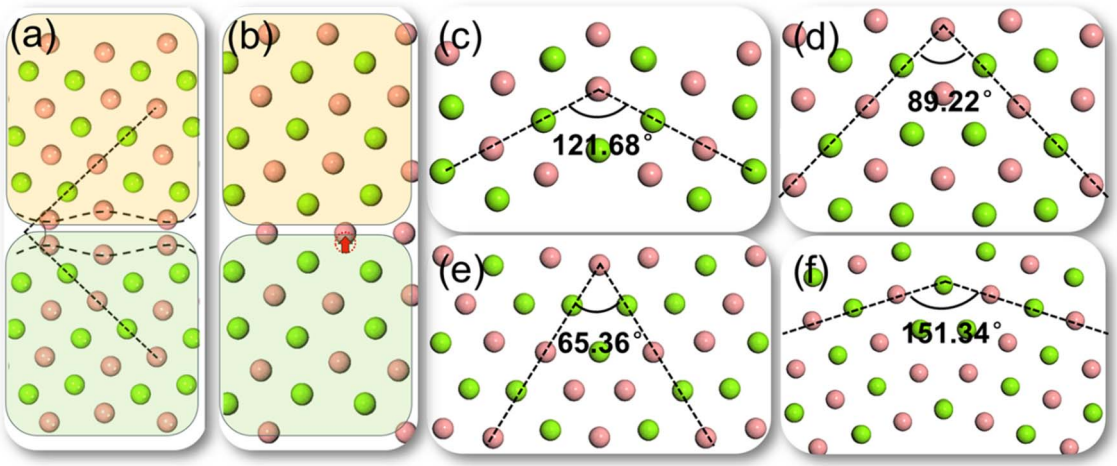

Fig. 1 (a) Corrugated interface of the {10$\bar{1}$2} TB; (b) construction of the {10$\bar{1}$2} TB with additional lattice shifts at the GB plane. (c)–(f) Schematic illustrations of the {10$\bar{1}$1}, {10$\bar{1}$2}, {10$\bar{1}$3}, and {20$\bar{2}$1} TBs, respectively. Green spheres represent the surface layer, and red spheres denote the subsurface layer.

the influence of periodic boundary conditions, we set vacuum layers of 2 nm above and 0.3 nm below the surface. During structural optimization, both atomic positions and lattice parameters underwent complete relaxation to attain stable configurations for the magnesium bulk and GBs. After full relaxation, the rotation angles of the obtained GB models are summarized in Table 1.

3.2 H adsorption on the GB surface

Extensive research efforts have been devoted to characterizing hydrogen adsorption characteristics on both pristine and doped magnesium surfaces. In a seminal study, Wu *et al.*[35] conducted a comparative adsorption analysis across four distinct magnesium systems—pristine, Pt-doped, defective, and oxidized surfaces—by sampling hydrogen adsorption configurations at characteristic high-symmetry sites (Atop, HCP, FCC, and Bridge). Their DFT calculations identified the FCC site as the most favorable adsorption locus, with hydrogen binding energies reaching 2.56 eV on pure magnesium surfaces. Remarkably, this adsorption preference persists for both oxide-modified and Pt-doped surfaces, with hydrogen adatoms consistently demonstrating site-specific affinity toward FCC coordination environments.

In our work, we constructed surface models of Mg (0001), four GBs and their grains. These models were used to systematically investigate the adsorption characteristics of hydrogen on their surface, providing a comprehensive comparison of adsorption behavior across different structural configurations. Interestingly, the traditional FCC and HCP sites do not exist at GBs and grain structures; they only have Atop, Bridge, and Hollow sites. Moreover, due to the existence of GBs, their structure differs from that of grains, and the special structure of GBs is likely to affect the adsorption energy. Therefore, we took this difference into account when calculating adsorption energy, and calculated all possible adsorption sites on GBs to study their adsorption characteristics.

For hydrogen atom adsorption at different surface sites, all H atoms were initially placed 0.2 nm away from the surface and allowed to move freely. After full relaxation, we determined the final adsorption positions and calculated the adsorption energies for different sites. First-principles calculations reveal consistent adsorption characteristics between the Mg (0001) surface (aligned with prior studies) and grain surfaces. On the Mg (0001) surface, hydrogen exhibits preferential stabilization at FCC sites. For the GB surface, excluding individual stable adsorbed Atop and Bridge sites, the dynamic relaxation trajectory shows that the hydrogen atom spontaneously migrated from the initial Atop/Bridge position to the adjacent Hollow position. Comparative adsorption energy analysis quantitatively corroborates this spatial preference, establishing Hollow sites as the most stable adsorption configurations on GB surfaces. The detailed site–energy correlations are systematically visualized in Fig. 2.

To elucidate the electronic origins of adsorption energy disparities, we performed atom-projected density of states (PDOS) analysis on the {10$\bar{1}$3} TB system, selecting this configuration as a prototypical TB model. The investigation specifically targeted adsorption sites (Atop, Bridge, and Hollow) to establish direct correlations between the local electronic structure and hydrogen adsorption energies. In Fig. 3, we present the projected density of states (PDOS) of the Mg s orbital and H s orbital at the Atop and Hollow sites near the Fermi level,

Table 1 Rotation angles of GBs after structural optimization

Index of crystal plane	Rotation angle (this work/°)	Rotation angle (literature/°)
(10$\bar{1}$3)	32.68	31.99 (ref. 33 and 34)
(10$\bar{1}$2)	44.61	43.11 (ref. 16, 33 and 34)
(10$\bar{1}$1)	60.84	61.91 (ref. 33 and 34)
(20$\bar{2}$1)	75.67	75.06 (ref. 33 and 34)

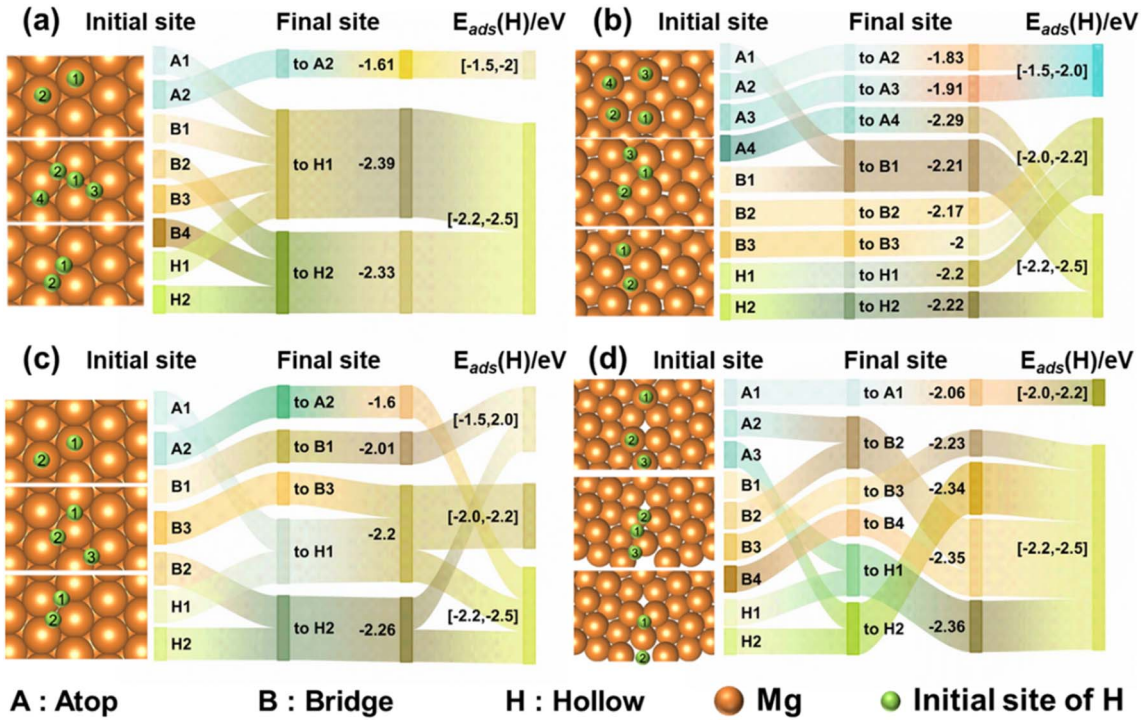

Fig. 2 The four Sankey diagrams correspond to (a) {10$\bar{1}$1}, (b) {10$\bar{1}$2}, (c) {10$\bar{1}$3}, and (d) {20$\bar{2}$1} TBs, respectively. The initial site on the left represents the location where the H atom was initially placed, and the final site represents the sites where the H atom was stably adsorbed after relaxation. The adsorption energy of each site to the H atom is linked with lines of the same color at the end of E_{ads}(H).

together with the corresponding charge density difference maps. The PDOS results reveal distinct differences in adsorption strength among the sites, with the overlap between Mg and H states near the Fermi level at the Hollow site being significantly stronger than at other sites. The charge redistribution upon adsorption is further illustrated by the charge density difference maps, which highlight the redistribution of electrons in the system due to interactions or bond formation.

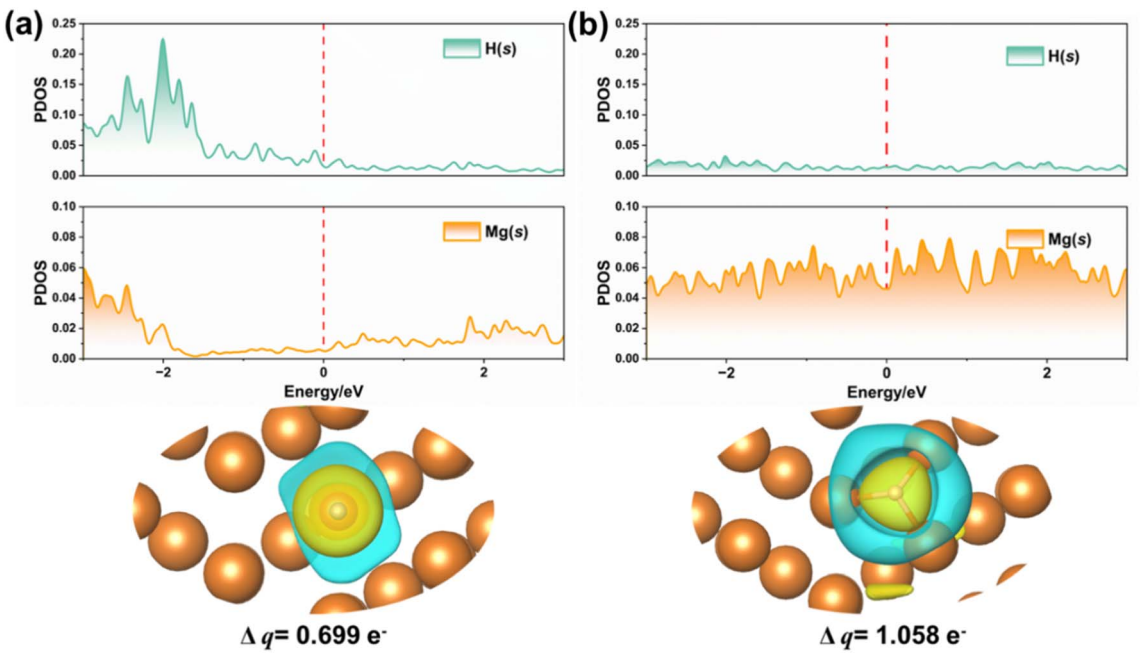

Fig. 3 (a) and (b) PDOS analysis and charge density difference maps at the Atop and Hollow sites of the {10$\bar{1}$3} TB, respectively. In the charge density difference maps, cyan regions indicate electron depletion, while yellow regions correspond to electron accumulation.

These maps clearly indicate the direction of electron transfer and the mode of electronic rearrangement during adsorption, thereby providing an intuitive explanation for the stronger adsorption at the Hollow site and the observed direction of Bader charge transfer.

3.3 Dissociation of H_2 on the GB surface

The hydrogen dissociation mechanism at GBs was investigated through a systematic computational protocol. In the initial state configuration, H_2 molecules were positioned $\geq$5 Å from GB surfaces to simulate pre-dissociation conditions. The final state was constructed by dissociating H_2 into two H adatoms, followed by full structural relaxation to their energy-minimized adsorption sites. Sequential geometry optimization employing conjugate gradient algorithms identified the lowest-energy configurations for both initial and dissociated states, thereby mapping the minimum energy pathway for hydrogen dissociation. During the dissociation process, the surface of the bottom GB was fixed to produce a higher energy barrier. Subsequently, we obtained the TS to understand the dissociation process through the CI-NEB method, but the CI-NEB method only mechanically inserted points between the initial state and the final state. Therefore, we further calculated the transition state using IDM and verified the virtual frequency and vibration direction of the TS to determine the accuracy of the TS. The dissociation pathway analysis incorporated geometric constraints by fixing the lower GB surface, which imposed an elevated energy barrier due to restricted atomic relaxation.

Extensive studies have been conducted on the dissociation of hydrogen on the Mg (0001) surface, with reported energy barriers ranging from 0.87 eV to 1.15 eV. Specifically, Vegge *et al.*[36] calculated a barrier of 1.15 eV, Banerjee *et al.*[37] reported 0.97 eV, Du *et al.*[38] and Wu *et al.*[35] obtained 1.05 eV, and Pozzo *et al.*[39] found a barrier of 0.87 eV. Ye *et al.*[40] calculated the dissociation energy barrier for the Mg $(10\bar{1}3)$ surface as 0.86 $\pm$ 0.1 eV. These theoretical values are in good agreement with the experimental value of 0.75 $\pm$ 0.15 eV.[41] However, the theoretical calculation part for studying the dissociation characteristics of H_2 on the GB surface is still very lacking.

Our systematic evaluation reveals the hydrogen dissociation energy barriers across three distinct configurations—the Mg (0001) surface, GBs, and isolated grains. Notably, the dissociation barrier determined for the Mg (0001) surface (1.13 eV) exhibits remarkable consistency with the value reported in Vegge *et al.*[36] (1.14 eV). This congruence between our result and established literature not only corroborates the precision of our DFT calculations but also reinforces the reliability of our comparative analysis framework for GB surfaces. The surfaces of the grains exhibit similarities to GBs, lacking FCC and HCP sites. As a result, the dissociation pathway on the grain surfaces was limited to two adjacent Hollow sites. The calculated dissociation energy barriers were 1.00 eV for the $\{10\bar{1}1\}$ grain, 0.75 eV for the $\{10\bar{1}2\}$ grain, 0.86 eV for the $\{10\bar{1}3\}$ grain and this is the same as Ye *et al.*[40] calculating the dissociation energy barrier for the Mg $(10\bar{1}3)$ surface (0.86 eV), 1.16 eV for the $\{20\bar{2}1\}$ grain. These values align with expectations, as the grain surfaces are essentially pure magnesium surfaces without any distinctive structural features.

When calculating the hydrogen dissociation energy barrier at GB surfaces, we specifically addressed their unique structural features. Unlike pristine magnesium surfaces, GB regions exhibited altered magnesium coordination environments. To account for this structural distinction, we systematically considered all geometrically possible dissociation sites. Guided by transition state theory principles, our analysis focuses on the minimum-energy barrier pathway, as the minimum-energy pathway represents the thermodynamically favored dissociation pathway. For each GB structure, we identified the key TS and created activation energy profiles (Fig. 4). The smallest energy barrier is found to be 0.74 eV on the $\{10\bar{1}1\}$ surface, 0.91 eV on the $\{10\bar{1}2\}$ surface, 0.93 eV on the $\{10\bar{1}3\}$ surface, and 0.97 eV on the $\{20\bar{2}1\}$ surface. Obviously, the energy barriers at these GBs do not uniformly promote the dissociation of H_2.

Through our analysis, most GBs in our work exhibit reduced dissociation energy barriers compared to the Mg (0001) surface, with only a few sites showing comparable values. Notably, when compared to their respective grain surfaces, the $\{10\bar{1}3\}$ and $\{10\bar{1}2\}$ TBs exhibit a higher H_2 dissociation energy barrier compared to their adjacent grain surface, suggesting preferential dissociation at the grain region rather than the GB interface.

Fig. 5 reveals a characteristic nonlinear dependence like a "reversed volcano": as the GB formation rotation angle progressively increases, the H_2 dissociation energy barrier on GB surfaces initially decreases, reaching a minimum before rising again. This demonstrates elevated activation thresholds for hydrogen dissociation at both small and large angles compared to intermediate-angle configurations. Our computational results are also consistent with *in situ* experimental observations in other HCP metals. Jia *et al.*[42] systematically investigated the precipitation behavior of hydrides at GBs in Zr, and their statistical analysis revealed that hydrides preferentially precipitate at boundaries with *c*-axis misorientation angles of $\approx$55–60°, whereas GBs at other angular ranges are less prone to hydride formation. This experimental trend is in excellent agreement with the "reversed volcano" relationship obtained in Mg, where medium-angle GBs were found to be most favorable for H_2 dissociation. These findings suggest that the proposed mechanism is not only valid for Mg but may also be generally applicable to a broader range of HCP metals. Moreover, GB surfaces exhibit substantially enhanced hydrogen dissociation reactivity compared to the Mg (0001) surface, especially the $\{10\bar{1}1\}$ TB, which exhibits exceptional activity, achieving 34.5% reduction in H_2 dissociation barrier compared to the Mg (0001) surface (1.13 $\rightarrow$ 0.74 eV) and 26% reduction relative to its grain surface (1.0 $\rightarrow$ 0.74 eV). This contrast underscores the critical role of the GB structure in modulating the energetics of hydrogen dissociation, highlighting its potential for enhancing the performance of magnesium-based hydrogen storage materials. This finding aligns with Martin *et al.*'s investigation of H_2 dissociation on the $\{11\bar{2}4\}$ TB.[43] Their computed barrier of 0.88 eV is markedly lower than that of Mg(0001) surfaces and further confirms the critical function of certain GB configurations in facilitating hydrogen dissociation through barrier reduction. As

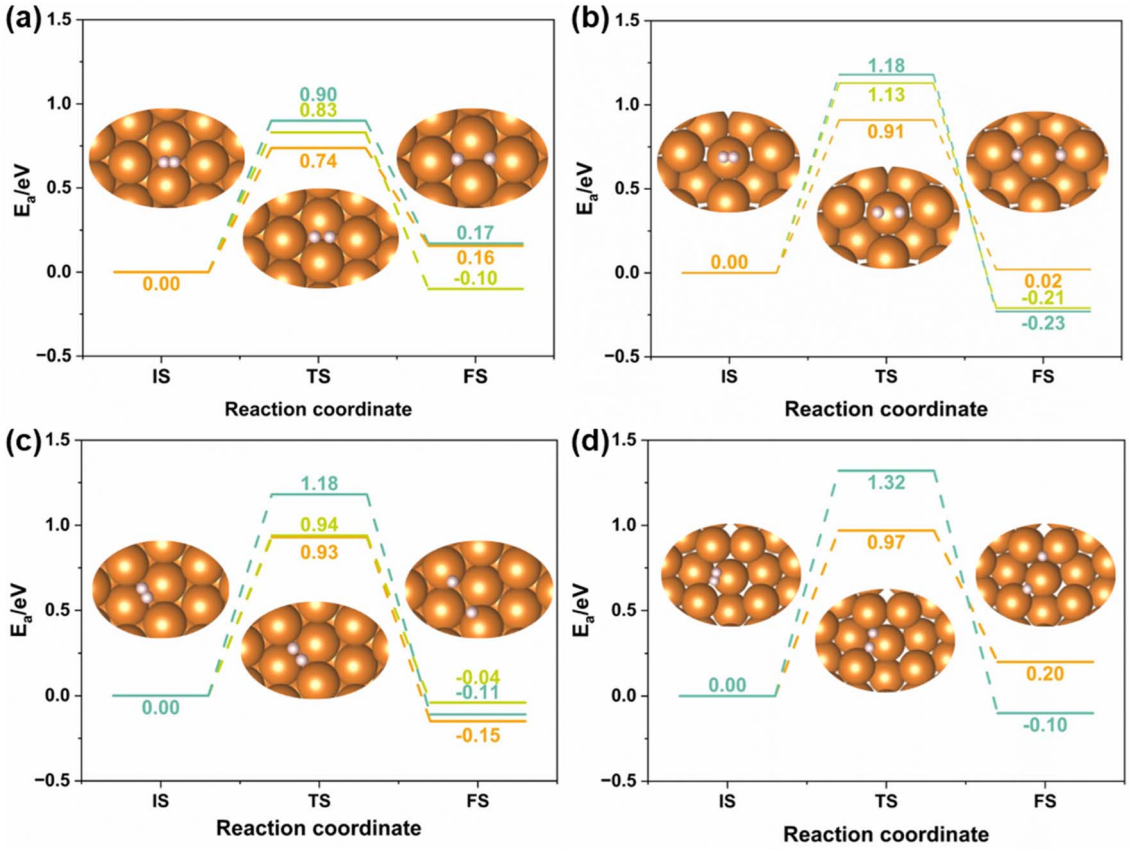

Fig. 4 Schematic representation of the hydrogen dissociation energy barrier on the (a) {10$\bar{1}$1}, (b) {10$\bar{1}$2}, (c) {10$\bar{1}$3}, and (d) {20$\bar{2}$1} TB surfaces.

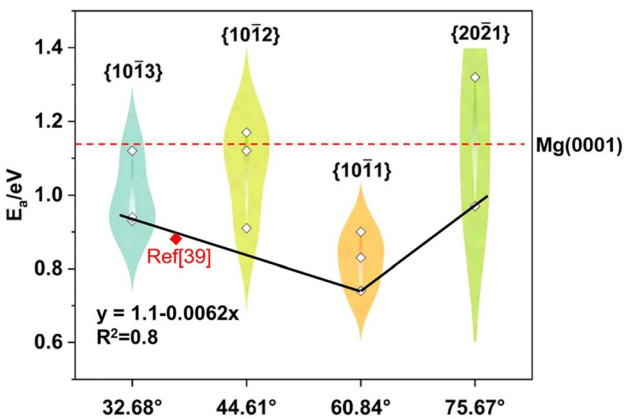

Fig. 5 Inverted volcano trend of dissociation energy barriers with angle variation.

shown in Fig. 5, the {11$\bar{2}$4} TB with a 35° rotation angle[44] also follows the angular relationship we identified. Our calculations confirm that both {10$\bar{1}$1} and {10$\bar{1}$2} TBs exhibit significantly lower hydrogen dissociation energy barriers than the {11$\bar{2}$4} TB and the Mg (0001) surfaces. Our calculations reveal a strong correlation between grain boundary rotation angles and H_2 dissociation barriers in Mg. Although constructing TBs with precise misorientation angles is experimentally challenging, several established methods exist. Angle-controlled TBs can be produced *via* directional solidification in a vertical Bridgman furnace using oriented seed crystals, or through diffusion bonding of single crystals cut to half the target angle (ϕ/2).[45,46] In addition, EBSD-guided selection and FIB micro-sample fabrication provide powerful routes for systematic, angle-resolved testing at the micro- and sub-micron scales. These experimental techniques offer a feasible pathway to validate our predicted angle–reactivity relationship, and we expect our findings to motivate future hydrogen storage studies on Mg TBs with controlled misorientations.[47]

The variation in energy barriers induced by these structural differences can be rationalized in terms of the Voronoi volume and CN. The Voronoi volume represents the spatial volume occupied by a Mg atom, which is often significantly enlarged at the GB. The CN denotes the number of nearest-neighbor atoms around a Mg atom, which tends to decrease at GBs due to irregular atomic packing. A larger local free volume together with a lower CN generally facilitates the approach of H atoms. Therefore, we calculated the Voronoi volume and CN of Mg atoms near each GB dissociation site and compared them with those on the pristine Mg surface, obtaining ΔV_{Vor} and ΔCN. We further performed a Pearson correlation coefficient (PCC) analysis by integrating all the calculated parameters to examine their correlations with the E_a of GBs (Fig. 6a). As shown in Fig. 6a, a clear correlation between these structural descriptors

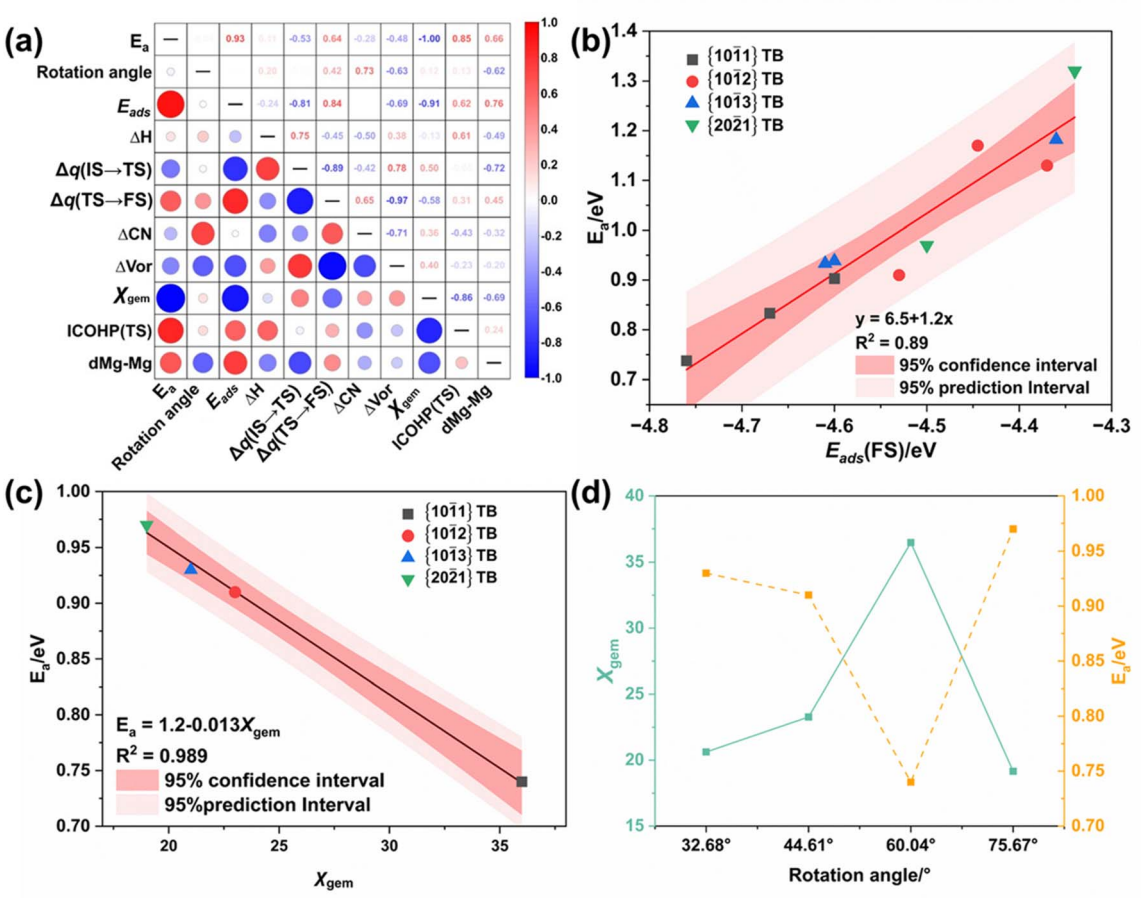

Fig. 6 Key interfacial mechanisms governing hydrogen dissociation: (a) correlation of site-specific adsorption energy (E_{ads}(H)) with charge transfer quantity of adsorbed state H; (b) influence of dissociated H adsorption energy (E_{ads}(FS)) on activation barriers (E_a); (c) relationship of TS charge transfer quantity and activation barriers (E_a); (d) relationship between the rotation angle and the hydrogen dissociation energy barrier and the average charge of magnesium at the GB surfaces.

and the dissociation barriers was observed. As noted above, ΔV_{Vor} and ΔCN act as geometric parameters that jointly influence the H_2 dissociation barriers. We therefore considered their combination with the barriers and tested several possible forms. Our fitting results reveal that, in our system, the product of ΔV_{Vor} and ΔCN exhibits the strongest linear correlation with the dissociation barrier. Accordingly, we defined χ_{gem} to quantify the barrier variation arising from structural differences:

$$E_a \propto \chi_{gem} = \Delta V_{Vor} \times \Delta CN \quad (2)$$

By fitting the data, we obtained the relation $E_a = 1.2 - 0.013\chi_{gem}$ ($R^2 = 0.99$). As shown in Fig. 6d, χ_{gem} first increases and then decreases with increasing rotation angle, indicating that χ_{gem} can serve as a geometry-driven descriptor to rationalize the origin of the volcano-type trend. Although the exact dissociation site on the {11$\bar{2}$4} TB reported by Martin *et al.* is not known, we attempted to construct this model and selected a representative site on the surface. The calculated χ_{gem} at this site is 26.51, and when substituted into our linear correlation, it gives a predicted dissociation barrier of 0.855 eV, which is very close to the reported value of 0.88 eV by Martin *et al.* This close agreement suggests that our descriptor may also have strong predictive capability for other GBs.

In Fig. 6b, we reveal a Brønsted–Evans–Polanyi (BEP) relationship between the dissociation barriers and adsorption energies. For the dissociation processes occurring at GBs, the transition-state energy is not completely independent of the reactants and products, but instead follows an approximately linear correlation ($E_a = 6.5 + 1.2E_{ads}$(FS), $R^2 = 0.89$). This indicates that a stronger adsorption ability of dissociated H atoms shifts the transition state closer to the final state, thereby lowering the energy barrier. Since the adsorption at the final state is largely governed by the charge distribution of surface atoms, the ability of χ_{gem} to account for the barrier variation can be understood in terms of the surface electronic distribution determined by the geometric structure. To further support the role of structural distortions, we quantitatively analyzed the Bader charge transfer along the IS → TS → FS pathway for all GBs (Table 2). Here, Δq denotes the amount of charge transferred from Mg atoms to H_2. A larger χ_{gem}, which reflects increased free volume and lower local coordination, facilitates

Table 2 χ_{gem} values, Bader charge transfer along the IS → TS → FS pathway, and ICOHP of TS for each GB

		Bader charge			
	χ_{gem}	Δq(IS → TS)	Δq(TS → FS)	Total Δq	ICOHP (TS)
$\{10\bar{1}1\}$	36.49	1.34	0.64	1.97	−0.19777
$\{10\bar{1}2\}$	23.28	1.01	0.67	1.68	−0.18485
$\{10\bar{1}3\}$	20.62	1.29	0.54	1.84	−0.15373
$\{20\bar{2}1\}$	19.16	1.16	0.67	1.83	−0.14382

more efficient electron donation into the H_2 σ* orbital. This trend is evident in the $\{10\bar{1}1\}$ TB, which exhibits both significant charge redistribution during the IS → TS step and the lowest dissociation barrier. By contrast, when the misorientation increases beyond 60°, χ_{gem} decreases, as in the $\{20\bar{2}1\}$ TB, leading to reduced electron transfer (Δq(IS → TS) = 1.16) and consequently a higher barrier.

While charge transfer analysis reveals the amount of electronic redistribution, it does not directly demonstrate whether the donated electrons contribute to bond stabilization at the TS. To address this, we evaluated the Mg–H interactions in the TS using the ICOHP. Although the H–H bond is not yet fully cleaved in the TS, a significant orbital interaction between H and neighboring Mg atoms is already present. The ICOHP provides a quantitative measure of this interaction strength, with more negative values indicating stronger Mg–H bonding tendencies and, therefore, a less stable H–H bond. Introducing ICOHP as a descriptor thus allows us to distinguish between mere charge accumulation and effective bonding interactions. Consistent with this interpretation, the $\{10\bar{1}1\}$ TB shows the most negative ICOHP value, confirming that efficient orbital overlap stabilizes the TS and facilitates H–H bond dissociation, whereas the $\{20\bar{2}1\}$ TB exhibits weaker Mg–H bonding, rationalizing its anomalously higher barrier.

Based on the above investigations, the key findings of this study are illustrated in the mechanistic diagram shown in Fig. 7. This figure presents the variation in hydrogen dissociation capability as a function of GB rotation angle. Three representative GBs were selected for detailed analysis, in which the ELF was employed to quantify both the initial surface electron distribution and the degree of electron localization following hydrogen adsorption and dissociation. As demonstrated in our prior work, the structural characteristics of GBs significantly influence the surface charge distribution, with the GB rotation angle being a critical determinant. Bader charge analysis reveals that the average charge density at the GB increases with the rotation angle and this trend is also evident in the ELF contour plots where darker regions correspond to higher electron localization. Moreover, the ELF analysis provides insights into the Mg–H charge transfer behavior, which, along with the surface electron density, plays a pivotal role in governing H_2 dissociation at the surface. Surfaces characterized by both high surface charge density and enhanced electron transfer capability are shown to facilitate hydrogen dissociation effectively.

Notably, the GB that optimally integrates both high surface charge density and strong electron transfer capability in our study is neither a high-angle nor a low-angle GB, but rather an intermediate-angle GB, which exhibits the greatest propensity to facilitate hydrogen dissociation.

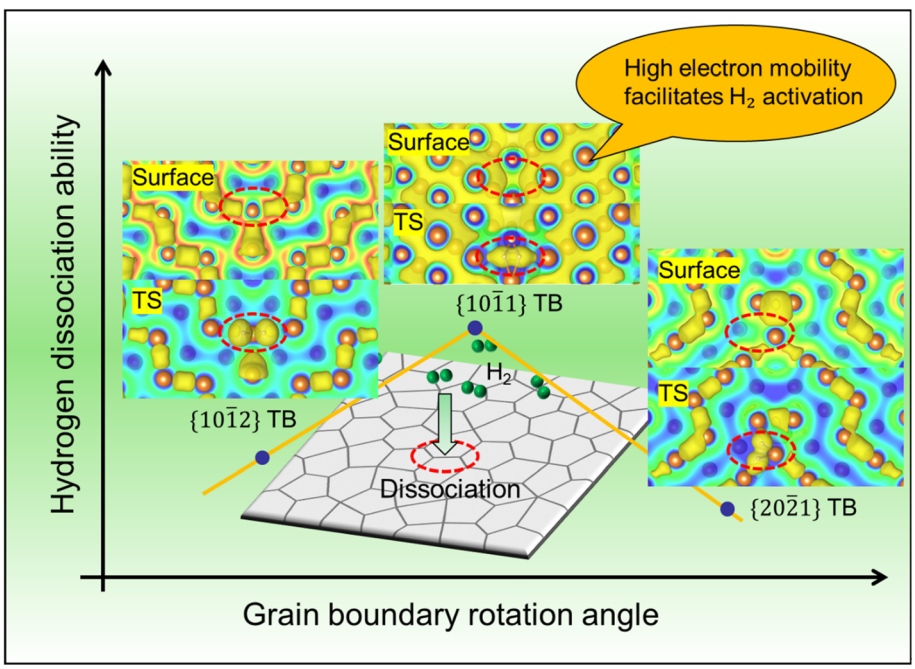

Fig. 7 Proposed mechanism of hydrogen dissociation at Mg GBs. The diagram integrates surface electron localization, Mg–H charge transfer, and structural features associated with different rotation angles, identifying intermediate-angle GBs as the most active sites for H_2 dissociation.

4 Conclusions

In summary, we performed first-principles calculations to uncover the mechanistic role of GBs in hydrogen adsorption and dissociation on magnesium. The dissociation barrier exhibits a reversed-volcano dependence on GB misorientation angle, with the $\{10\bar{1}1\}$ TB presenting the lowest barrier while the high-angle $\{20\bar{2}1\}$ TB shows an anomalous increase. To rationalize this behavior, we introduced a geometry-based descriptor χ_{gem}, which quantitatively correlates GB structural distortions with reactivity ($R^2 \approx 0.99$). This descriptor not only explains the volcano-type trend but also resolves the exceptional behavior of the $\{20\bar{2}1\}$ TB. Thermodynamic validation through a BEP relationship and electronic analysis *via* Bader charge transfer and TS-ICOHP further demonstrated that χ_{gem} governs hydrogen activation by simultaneously modulating adsorption strength, electron redistribution, and transition-state stabilization.

This study establishes χ_{gem} as a simple yet effective descriptor linking atomic-scale geometry to the electronic structure and catalytic performance at GBs. Beyond rationalizing hydrogen activation in Mg, the framework may be transferable to other lightweight metals and hydrides, providing new insights for grain boundary engineering. Looking forward, the integration of machine-learning potentials with DFT will enable the exploration of larger and more diverse GB configurations, thereby allowing statistical sampling that better mirrors experimental microstructures. Moreover, *in situ* spectroscopic or microscopic observations of hydrogen at GBs would provide essential validation of our predictions. Such combined theoretical and experimental efforts will further advance the rational design of Mg-based hydrogen storage materials with enhanced kinetics.

Conflicts of interest

There is no conflict of interest to declare.

Data availability

The data supporting this article have been included as part of the Supplementary Information (SI). See DOI: **https://doi.org/10.1039/d5ta04858c**.

Acknowledgements

The authors gratefully acknowledge financial support for this work from the Natural Science Foundation of Hebei (Grant No. E2023502006) and Fundamental Research Fund for the Central Universities (2025MS131).

References

1 M. Dornheim, S. Doppiu, G. Barkhordarian, U. Boesenberg, T. Klassen, O. Gutfleisch and R. Bormann, *Scr. Mater.*, 2007, **56**, 841–846.
2 I. P. Jain, C. Lal and A. Jain, *Int. J. Hydrogen Energy*, 2010, **35**, 5133–5144.
3 Y. Pang, Y. Liu, M. Gao, L. Ouyang, J. Liu, H. Wang, M. Zhu and H. Pan, *Nat. Commun.*, 2014, **5**, 3519.
4 X. Zhang, S. Ju, C. Li, J. Hao, Y. Sun, X. Hu, W. Chen, J. Chen, L. He, G. Xia, F. Fang, D. Sun and X. Yu, *Nat. Commun.*, 2024, **15**, 2815.
5 H. T. Uchida, S. Wagner, M. Hamm, J. Kürschner, R. Kirchheim, B. Hjörvarsson and A. Pundt, *Acta Mater.*, 2015, **85**, 279–289.
6 Y. Wang, X. Chen, H. Zhang, G. Xia, D. Sun and X. Yu, *Adv. Mater.*, 2020, **32**, 2002647.
7 X. Zhang, C. Li, J. Ye, X. Hu, W. Chen, F. Fang, D. Sun, Y. Liu, X. Yu and G. Xia, *J. Am. Chem. Soc.*, 2025, **147**, 2786–2796.
8 X. Zhang, Y. Sun, S. Ju, J. Ye, X. Hu, W. Chen, L. Yao, G. Xia, F. Fang, D. Sun and X. Yu, *Adv. Mater.*, 2023, **35**, e2206946.
9 X. Hu, X. Chen, X. Zhang, Y. Meng, G. Xia, X. Yu, D. Sun and F. Fang, *Adv. Sci.*, 2024, **11**, e2400274.
10 W. J. Botta, G. Zepon, T. T. Ishikawa and D. R. Leiva, *J. Alloys Compd.*, 2022, **897**, 162798.
11 A. H. M. Krom and A. Bakker, *Metall. Mater. Trans. B*, 2000, **31**, 1475–1482.
12 A. Oudriss, J. Creus, J. Bouhattate, E. Conforto, C. Berziou, C. Savall and X. Feaugas, *Acta Mater.*, 2012, **60**, 6814–6828.
13 J. Karst, F. Sterl, H. Linnenbank, T. Weiss, M. Hentschel and H. Giessen, *Sci. Adv.*, 2020, **6**, eaaz0566.
14 Y. Chino, D. Nishihara, T. Ueda and M. Mabuchi, *Mater. Trans.*, 2011, **52**, 1123–1126.
15 M. Yuasa, D. Nishihara, M. Mabuchi and Y. Chino, *J. Phys.: Condens. Matter*, 2012, **24**, 085701.
16 G. Gengor, A. S. K. Mohammed and H. Sehitoglu, *Acta Mater.*, 2021, **219**, 117256.
17 G. Kresse and D. Joubert, *Phys. Rev. B: Condens. Matter Mater. Phys.*, 1999, **59**, 1758–1775.
18 S. Grimme, J. Antony, S. Ehrlich and H. Krieg, *J. Chem. Phys.*, 2010, **132**, 154104.
19 G. Henkelman and H. Jónsson, *J. Chem. Phys.*, 2000, **113**, 9978–9985.
20 G. Henkelman, B. P. Uberuaga and H. Jónsson, *J. Chem. Phys.*, 2000, **113**, 9901–9904.
21 A. Heyden, A. T. Bell and F. J. Keil, *J. Chem. Phys.*, 2005, **123**, 224101.
22 C. Riplinger and E. A. Carter, *J. Phys. Chem. C*, 2015, **119**, 9311–9323.
23 A. Stukowski, *Modell. Simul. Mater. Sci. Eng.*, 2010, **18**, 015012.
24 K. Momma and F. Izumi, *J. Appl. Crystallogr.*, 2011, **44**, 1272–1276.
25 V. Wang, N. Xu, J.-C. Liu, G. Tang and W.-T. Geng, *Comput. Phys. Commun.*, 2021, **267**, 108033.
26 J. W. Christian and S. Mahajan, *Prog. Mater. Sci.*, 1995, **39**, 1–157.
27 P. Partridge, *Metall. Rev.*, 1967, **12**, 169–194.
28 J. P. Hirth, R. C. Pond, R. G. Hoagland, X. Y. Liu and J. Wang, *Prog. Mater. Sci.*, 2013, **58**, 749–823.
29 J. Li, M. Sui and B. Li, *Acta Mater.*, 2021, **216**, 117150.
30 Y. Liu, N. Li, S. Shao, M. Gong, J. Wang, R. J. McCabe, Y. Jiang and C. N. Tomé, *Nat. Commun.*, 2016, **7**, 11577.

31 J. Wang, I. J. Beyerlein and C. N. Tomé, *Int. J. Plast.*, 2014, **56**, 156–172.
32 R. Mahjoub, M. Ferry and N. Stanford, *Comput. Mater. Sci.*, 2022, **210**, 111042.
33 C. Xu, X. Tian, W. Jiang, Q. Wang and H. Fan, *Int. J. Plast.*, 2022, **156**, 103362.
34 J. Wang and I. J. Beyerlein, *Modell. Simul. Mater. Sci. Eng.*, 2012, **43**, 3556–3569.
35 G. Wu, J. Zhang, Y. Wu, Q. Li, K. Chou and X. Bao, *Appl. Surf. Sci.*, 2009, **256**, 46–51.
36 T. Vegge, *Phys. Rev. B: Condens. Matter Mater. Phys.*, 2004, **70**, 035412.
37 S. Banerjee, C. G. S. Pillai and C. Majumder, *J. Phys. Chem. C*, 2009, **113**, 10574–10579.
38 A. J. Du, S. C. Smith, X. D. Yao and G. Q. Lu, *J. Phys. Chem. B*, 2006, **110**, 1814–1819.
39 M. Pozzo and D. Alfè, *Int. J. Hydrogen Energy*, 2009, **34**, 1922–1930.
40 J.-H. Ye, Y.-J. Zhao, Y.-X. Fang, H.-J. Lin, L. Bai and J.-J. Tang, *Int. J. Hydrogen Energy*, 2019, **44**, 4897–4906.
41 M. Johansson, C. W. Ostenfeld and I. Chorkendorff, *Phys. Rev. B: Condens. Matter Mater. Phys.*, 2006, **74**, 193408.
42 Y.-J. Jia, I. J. Beyerlein and W.-Z. Han, *Acta Mater.*, 2021, **216**, 117146.
43 M. Panholzer, M. Obermayer, I. Bergmair and K. Hingerl, *Int. J. Hydrogen Energy*, 2015, **40**, 5683–5688.
44 Y. Chong, M. Poschmann, R. Zhang, S. Zhao, M. S. Hooshmand, E. Rothchild, D. L. Olmsted, J. W. Morris, D. C. Chrzan, M. Asta and A. M. Minor, *Sci. Adv.*, 2020, **6**, eabc4060.
45 K. Bissa, T. Al-Samman and D. A. Molodov, *Crystals*, 2024, **14**, 130.
46 N. Malyar, H. Springer, J. Wichert, G. Dehm and C. Kirchlechner, *Mater. Test.*, 2019, **61**, 5–18.
47 K. Bissa, T. Al-Samman and D. A. Molodov, *J. Magnesium Alloys*, 2023, **11**, 1556–1566.